

Dual Resonant Sum Frequency Generations from Two-Dimensional Materials

Youngjae Kim, Hyunmin Kim,* Houk Jang, Jong-Hyun Ahn, and J.D. Lee*

Cite This: *Nano Lett.* 2020, 20, 4530–4536

Read Online

ACCESS |



Metrics & More



Article Recommendations



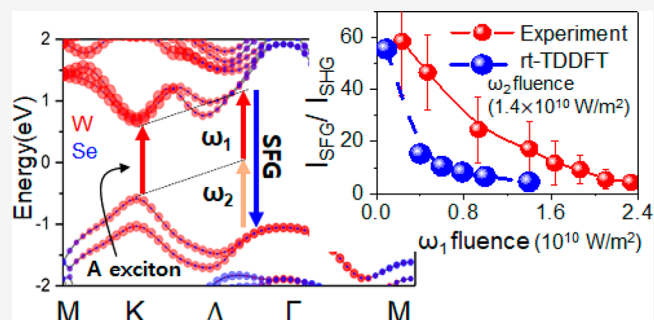
Supporting Information

ABSTRACT: We propose dual resonant optical sum frequency generation (SFG), where the two most singular resonances could be selected, and report for the monolayer (1L-) WSe₂ when one (ω_1) of two excitation pulses is resonant to A exciton and their sum frequency ($\omega_1 + \omega_2$) to D exciton. The dual resonant SFG confirms that, under an irradiation of ω_1 and ω_2 pulses with the same fluence of $\sim 1.4 \times 10^{10}$ W/m², its signal intensity could be enhanced about 20 times higher than the resonant SHG (i.e., $2\omega_1$ to the D excitonic absorption). Further, the dual resonant SFG intensity of 1L-WSe₂ is found to be 1 order of magnitude higher than the single resonant SFG intensity of 1L-WSe₂ under the same condition of two-pulse irradiation. Finally, observations of the dual resonant SFG are thoroughly examined using real-time time-dependent density functional theory (rt-TDDFT), and the relevant nonlinear optical characteristics are scrutinized using the Greenwood–Kubo formalism.

KEYWORDS: SFG, dual resonance, excitonic resonance, TMD, rt-TDDFT

INTRODUCTION

Nonlinear optical second harmonic generation (SHG), which originates from the noncentrosymmetric crystal structure, and the related spectroscopy and microscopy have been powerful for an attainment of the knowledge of van der Waals layered materials and atomically thin transition-metal dichalcogenides (TMDs). In particular, the importance and potentiality of SHG in TMDs has been deeply envisaged in its colossal response to the incident excitation pulse. The second-order nonlinear optical susceptibility $\chi_{\text{SHG}}^{(2)}$ at the level of 5 nm/V was first reported in the exfoliated monolayer (1L-) MoS₂,¹ which is approximately three orders of magnitude higher than that in the typical nonlinear optical response of beta-barium borate (β -BaB₂O₄ or BBO) crystal.² Here, in 1L-MoS₂, a constructive summation of the second harmonic polarization induced by the dipole moments in the broken inversion symmetry center^{3,4} is gigantically amplified by the resonant amplification process via the two-photon mediated absorption near 3 eV region (C exciton).^{5,6} Subsequently, similar nonlinear optical susceptibilities are also reported for tungsten-based TMDs, that is, 5 nm/V for 1L-WSe₂⁷ and 4.5 nm/V for 1L-WSe₂.⁸ Further, for 1L-WSe₂, a strong enhancement of SHG at the resonance to A exciton at $T = 4$ K⁹ and the Fano-like quantum interference in SHG¹⁰ due to combination of electric and magnetic dipole moments have been reported. Beyond SHG, sum frequency generation (SFG) with more explicit phase-matched linear combination of two different frequencies was also reported in layered MoS₂ and related heterosystems using



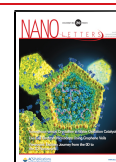
band-filtered supercontinuum illumination.¹¹ It is only very recent that SFG from monolayer and heterobilayer TMD structures can be utilized for the wavelength-dependent spectroscopy and the spatial microscopic imaging, where the frequency summation of two continuous waves (CWs) is achieved with the CW laser fluences of $\sim 10^{10}$ W/m², typically three orders of magnitude lower than pulse-based fluence.¹²

Theoretical investigation of a real-time evolution of the nonlinear current enables to understand various excitation paths for harmonic generations and estimate the resulting amplitudes of harmonic generations through the microscopic quantum mechanics of solids, which have been extensively performed based on the two-band model^{13,14} and the real-time time-dependent density functional theory^{15–19} (rt-TDDFT). For instance, the study of harmonic generations in TMDs has successfully delivered the physical insight for a practical control of two-color-dressed harmonic yields within the first-principles level¹⁶ as done in the case of layered systems such as h-BN²⁰ and even topological matters.²¹ However, interactions between harmonics under the two-color optical excitations are still veiled, especially in the multiple excitonic band structure as is

Received: March 30, 2020

Revised: May 17, 2020

Published: May 18, 2020



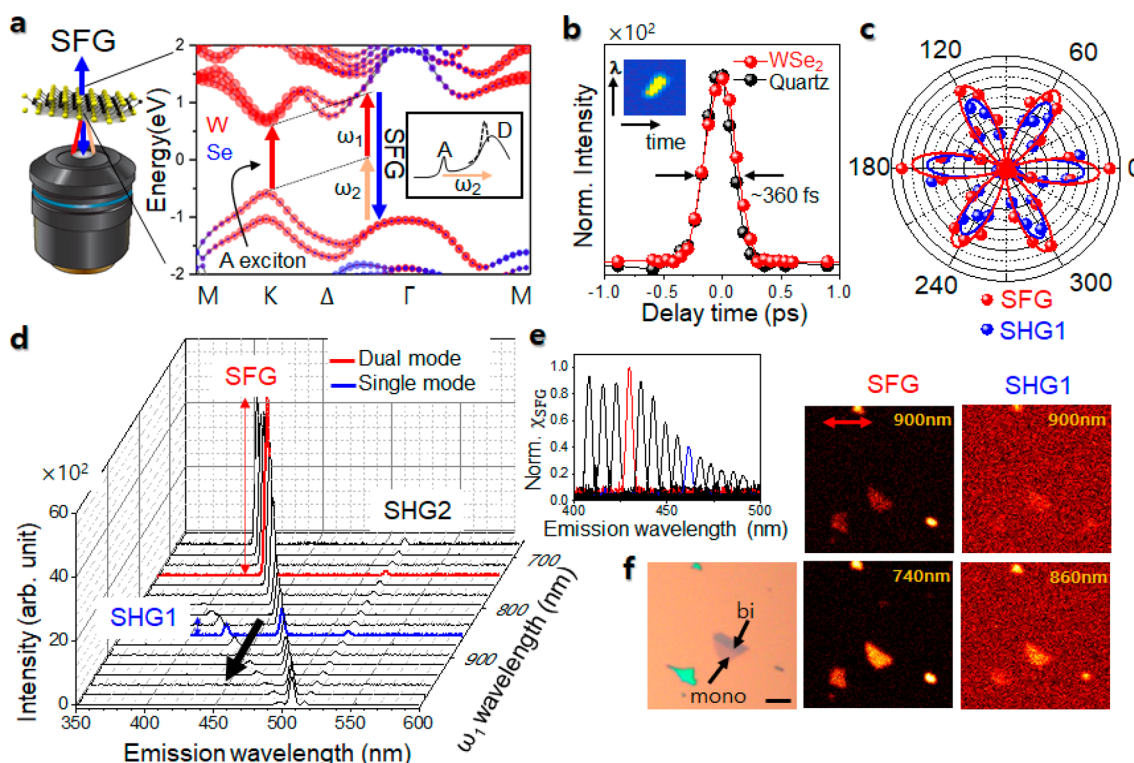


Figure 1. Dual resonant SFG spectroscopy and imaging. (a) Schematic illustration of the dual resonant condition of two excitation pulses ω_1 (red) and ω_2 (apricot) for the sum frequency generation (SFG, blue) from 1L-WSe₂. A and D mean A and D excitons, respectively. Inset represents an additional enhancement in the susceptibility caused by the possible dual resonance effect (dotted peak). (b) Normalized time-overlap SFG from 1L-WSe₂ (red) and quartz wafer (black) by mixing 1040 and 860 nm pulses as a function of the delay time. (c) Polarization-dependent signals between SFG and SHG from 1L-WSe₂. (d) Emission spectra from 1L-WSe₂ under a simultaneous illumination of a wavelength-fixed pulse (ω_2 , 1040 nm) and a wavelength-varying pulse (ω_1 , 680–1000 nm). (e) Normalized SFG susceptibility (each spectrum of SFG is projected toward the direction of black arrow of (d)). (f) Optical, SFG, and SHG images with regard to the wavelength of the ω_1 pulse. The black scale bar in the optical image is 10 μm . Double-sided red arrow represents the polarization direction of two incident pulses and analyzer. Fluences of the ω_1 and ω_2 pulses are given by $\sim 1.4 \times 10^{10} \text{ W/m}^2$ unless mentioned otherwise.

usually found in TMDs. Meanwhile, it is useful to employ the decomposed optical conductivity tensor obtained by the Greenwood–Kubo formalism,²² from which the second-order nonlinear optical response have been constructed for a complete description of the nonlinear nature of TMDs. Mannebach et al. have studied the time-resolved SHG from 1L-MoS₂,²³ where they have theoretically combined the first-order response of each excitation pulse and attained the electronically sensitive SHG signal. Here, we try to reach the SFG excitation in a similar fashion to the stimulated emission depletion for the super-resolution fluorescence imaging^{24,25} and the defect- or phonon-assisted second-order Raman spectroscopy.^{26–28}

In this work, we demonstrate the two-color optical SFG from 1L-WSe₂ in a dual resonant mode where one (ω_1) of the two colors is tuned to A exciton ($\sim 1.68 \text{ eV}$) and their sum frequency ($\omega_1 + \omega_2$) to the D exciton ($\sim 2.87 \text{ eV}$). The dual resonant SFG has an evident merit that the two most singular resonances could be selected, which is sharply contrasted to the selection-not-permitted SHG. Consequently, the dual resonant SFG confirms that, under the same fluence exposure ($\sim 1.4 \times 10^{10} \text{ W/m}^2$) of the ω_1 and ω_2 pulses, the signal intensity could be about 20 times higher than the resonant SHG (i.e., $2\omega_1$ resonant to D exciton). Further, the dual resonant SFG intensity of 1L-WSe₂ ($\chi_{\text{SHG}}^{(2)} = 23 \text{ nm/V}$) is found to be one order of magnitude higher than the single resonant SFG intensity of 1L-WSe₂ ($\chi_{\text{SHG}}^{(2)} = 6.7 \text{ nm/V}$) which lacks the A

excitonic resonance. The dual resonant SFG is explicitly examined with theoretical models of a selective combination of two singular resonances using the first-principles calculation. Also, the momentum transfer efficacy in 1L-WSe₂ and 1L-WSe₂ is discussed through their nonlinear optical characteristics in the two-dimensional reciprocal space using the Greenwood–Kubo formalism. Our proposition of the dual resonant SFG would provide new scientific insights not only to the nonlinear spectroscopy and microscopy but also the nonlinear optics and technology using the two-dimensional semiconductors.

RESULTS AND DISCUSSION

Figure 1a depicts a schematic representing the dual resonant sum frequency generation (SFG) from WSe₂ atomic monolayer when one frequency (ω_1) of two illumination beams is tuned to A exciton and their sum frequency ($\omega_1 + \omega_2$) is tuned to D exciton. Several combinations for the dual resonance SFG are available because there are observed four excitonic absorption bands labeled A, B, C, and D excitons²⁹ along the K–Γ line in the electronic structure of 1L-WSe₂. Let us note that, as shown in the illustration, A and D excitons would be most singular in that the former is optically primary at the direct band gap and the latter is notably robust due to the band nesting. A signal enhancement according to the coupled dual resonance is schematically illustrated as an extra susceptibility increment (dotted peak) in the inset.

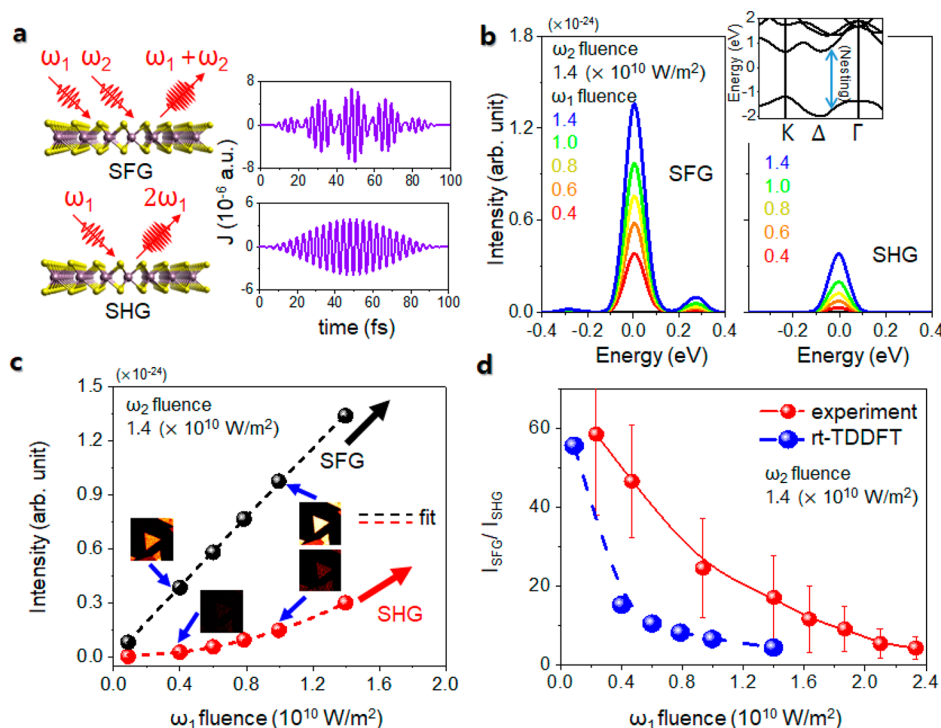


Figure 2. Dual resonant SFG and SHG from experiment and theory. (a) Schematics of SFG and SHG and nonlinear oscillation of the real-time current density from rt-TDDFT, where a.u. means the atomic unit. (b) SFG and SHG spectra evaluated from rt-TDDFT with respect to the ω_2 -pulse fluence. The D excitonic absorption energy at the band nesting near the Δ point (inset) is set to 0 eV. (c) Spectral intensity of SFG and SHG as a function of the ω_1 -pulse fluence. SFG is found to have a linear dependence whereas SHG a quadratic dependence. Pieces of inset images are taken from MBE-grown 1L-WSe₂ triangles at the corresponding fluence conditions indicated by blue arrows. (d) Ratio of spectral intensities between SFG and SHG from experiment and rt-TDDFT with respect to the ω_1 -pulse fluence. Note that wavelengths of the ω_1 and ω_2 pulses are taken to be 740 and 1040 nm for SFG, respectively, and that of the ω_1 pulse 860 nm for SHG.

Concerning the microscopy setup, details are introduced in our previous works.^{30,31} Briefly, a spatiotemporal overlap of two femtosecond pulses via the oil immersion lens was experimentally achieved using the dual mode optical parametric oscillator equipped to the inverted-type raster-scanning microscopy. First, we evaluate the SFG property by tracing the time-overlap of two pulse trains and in Figure 1b compare SFG between 1L-WSe₂ on the quartz wafer when we mix a 840 nm 120 fs pulse and a 1040 nm 220 fs pulse. Time-resolved SFG is well-displayed by approximately 360 fs of fwhm (full-width-at-half-maximum) in the time overlap profiles from 1L-WSe₂ and quartz substrate, whose beam chirping (due to the quartz substrate) is directly perceived in the inset figure. See also the Mach–Zehnder type CARS (coherent anti-Stokes Raman scattering) interferometry³² to unambiguously identify the time-dependent cross-correlation of two excitation pulses taken after splitting 740 nm pulses into two in the Supporting Information. It is also notable that the SFG intensity of 1L-WSe₂ ($\sim 1.4 \times 10^{10}$ W/m² for each pulse) is more than one order magnitude higher than that of the quartz substrate regardless of the used fluence ($\sim 1.4 \times 10^{11}$ W/m² for each pulse), addressing an approximately five orders of magnitude difference in the SFG susceptibility. Figure 1c displays the polarization dependence of SFG together with SHG when the sample was rotated against the fixed polarization of incident pulses and analyzer. In this case, the 2H-WSe₂ monolayer belongs to the D_{3h} point group where the polarized SHG light follows $\cos 3\theta$ dependence with the fundamental polarization angle θ , showing a 6-fold lobe pattern as displayed in Figure 1c. Here, the scale was normalized with a slight relative adjustment

for visibility and no discernible phase mismatches between SFG and SHG signals were found.

Figure 1d shows the five-time-averaged emission spectra achieved by mixing a wavelength-varying (680–1000 nm) excitation pulse (ω_1) and a 1040 nm pulse (ω_2) with the fluence of $\sim 1.4 \times 10^{10}$ W/m² for both. It should be noted that the measurement below 400 nm is highly deteriorated by the silver mirror component (PF10-03-P01, Thorlabs) which limitedly reflects the light in the near UV region. A comparison of the spectral intensity between SFG and SHG is straightforwardly demonstrated; the maximum SFG intensity (marked as SFG in red) is obtained at 432 nm (2.87 eV) when a 740 nm pulse ($\omega_1 = 1.68$ eV) is mixed with a 1040 nm ($\omega_2 = 1.19$ eV) pulse, while the maximum SHG intensity (marked as SHG1 in blue) is shown at 430 nm (2.88 eV) by the 860 nm ($\omega_1 = 1.44$ eV) excitation pulse. On the other hand, SHG2 (at 520 nm) maintains almost the constant intensity level for each wavelength-dependent spectrum. For more quantitative analysis, we obtain the SFG susceptibility ($\chi_{\text{SFG}}^{(2)}$) from the solution of Green's function with respect to the infinite two-dimensional sheet source which was revamped for two different excitation frequencies (ω_1, ω_2) as follows:⁸

$$\chi_{\text{SFG}}^{(2)} = \frac{\epsilon_0 c \lambda_{\text{SFG}}^4 P_{\text{SFG}} R t_{\omega_1} t_{\omega_2} (n_{\omega_{\text{SFG}}} + 1)^2 (n_{\omega_1} + 1)^2 (n_{\omega_2} + 1)^2}{32 N A^2 t_{\text{SFG}} P_{\omega_1} P_{\omega_2} \phi} \quad (1)$$

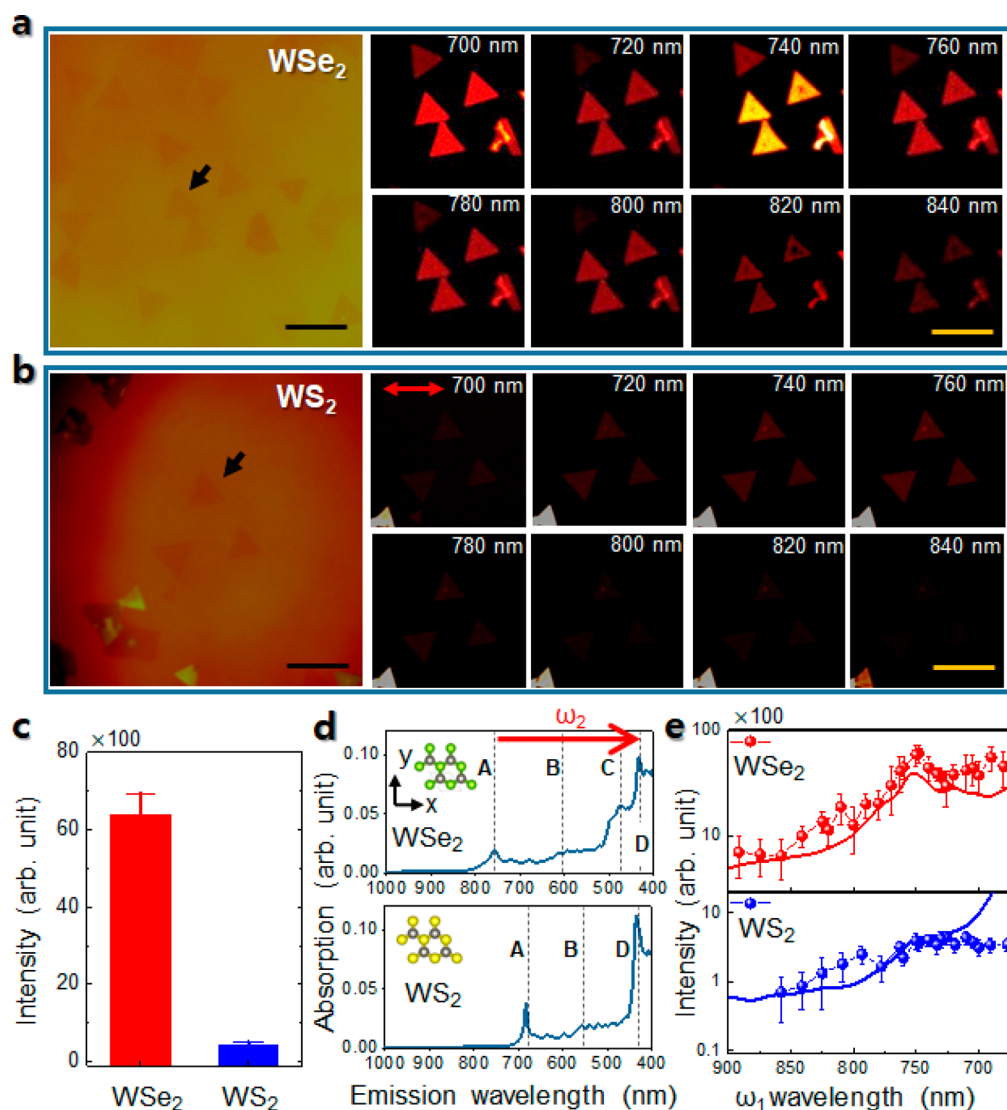


Figure 3. Dual resonant SFG for 1L-WSe₂ and single resonant SFG for 1L-WS₂. (a, b) Optical images (big-sized images in the left panel) and SFG images (small-sized images in the right panel) for 1L-WSe₂ and 1L-WS₂ with respect to the ω_1 -pulse wavelength under a fixed 1040 nm (ω_2 -pulse) irradiation. Black and yellow scale bars are 20 μ m. Double-sided red arrow means the polarization direction of two incident pulses and analyzer. Raman spectra of the monolayers pointed by black arrows are available in the [Supporting Information](#). (c) SFG spectral intensity for 1L-WSe₂ and 1L-WS₂ under the 740 nm (ω_1 -pulse) and 1040 nm (ω_2 -pulse) illumination. (d) Optical absorption spectra of 1L-WSe₂ and 1L-WS₂ evaluated from $\text{Im}[\chi_{yy}(\omega)]$ within the Greenwood–Kubo linear response theory. (e) Experimental (dots) and theoretical (lines) SFG intensity profiles from 1L-WSe₂ (red) and 1L-WS₂ (blue) with respect to the ω_2 -pulse wavelength. Fluences of the ω_1 and ω_2 pulses are fixed to be $\sim 1.4 \times 10^{10}$ W/m². The large discrepancy between experiment and theory at short wavelengths for WS₂ is discussed in the [Supporting Information](#).

Here, ϵ_0 is the vacuum permittivity, c the speed of light, R the repetition rate of the pulse train (80 MHz), NA the numerical aperture of the objective lens (1.35), and ϕ the solid angle of the scattered beam. Also, λ is the wavelength, P the intensity, t the pulse width, and n the refractive index of the substrate³³ with regard to the indicated incident or generated photon. Figure 1e gives the normalized $\chi_{\text{SHG}}^{(2)}$ (as for 740 nm) from eq 1 for each spectrum of Figure 1d which is subtracted with the time-mismatching between ω_1 and ω_2 pulses. In this respect, the ratio of the second-order nonlinear optical susceptibility between SFG and SHG ($\chi_{\text{SFG}}^{(2)}/\chi_{\text{SHG}}^{(2)}$) is obtained as 2.0 for $\omega_1 = 860$ nm and 4.6 for $\omega_1 = 740$ nm illumination in a simultaneous presence of 1040 nm pulse (see more details in the [Supporting Information](#)). Eventually, $\chi_{\text{SHG}}^{(2)}$ of 1L-WSe₂ can be experimentally determined to be 10 nm/V and 23 nm/V as in the two pulse mixing condition above, i.e., $\omega_1 = 860$ and 740

nm. For clarity, Figure 1f shows SFG and SHG images of the exfoliated 1L-WSe₂ with respect to the pulse wavelengths of Figure 1d. In particular, the SFG image demonstrates a better signal-to-noise level than the SHG image at the 740 nm excitation in a monolayer selective fashion. Compared with the bilayer system, a recovery of the centrosymmetry in the single 2H-type stacking structure is also strictly managed as the odd parity within approximately four orders of the SFG signal range (0.008%; finite optical phase shift at the interface).³⁴ It is interesting to generally test the superiority of the dual resonant SFG over the single resonant SFG, which is not immediately available due to our limitation on independently tunable light sources. Instead, a theoretical demonstration is provided in Figure S8.

To more deeply discuss the dual resonant SFG, we employ the first-principles rt-TDDFT implemented in ELK code (see

more details in the [Supporting Information](#)) in solving the time-dependent Schrödinger equation within a periodic unit cell structure of 1L-WSe₂. In [Figure 2a](#), we simulate a generation of the electric current density from the time evolution of Kohn–Sham orbitals in cases of SFG and SHG where ω_1 and ω_2 pulses are long enough to drive solid electrons into excited states. The current density of SFG is shown to have nonlinear frequencies mixed with various sums of oscillations; however, that of SHG has a monochromatic nonlinear behavior with a single oscillation. In [Figure 2b](#), spectra of SFG or SHG are delivered from the relevant Fourier components of the real-time current density oscillation. Especially, we focus on the band nesting position near the Δ point, i.e., the D excitonic absorption, where the sum frequency $\omega_1 + \omega_2$ is absorbed in SFG or the second harmonic $2\omega_1$ in SHG. A typical linear increase of the SFG signal intensity is obtained with respect to the fluence of the ω_1 pulse for a fixed fluence of the ω_2 pulse $\sim 1.4 \times 10^{10}$ W/m², whereas a quadratic increase of the SHG intensity is obtained. This results in a sizable intensity difference between SFG and SHG, and consequently, the observed imaging at the band nesting, i.e., at D exciton, would strongly depend on whether it is taken by SFG or SHG, which is clearly revealed in [Figure 2c](#). In fact, several experimental images taken in the microscopy of SFG or SHG are provided as insets [Figure 2c](#), where the SFG images are evidently clearer than the SHG ones, consistent with the calculation. A numerical comparison of nonlinear signals, for instance, a ratio of SFG and SHG intensities, between experiment and calculation is depicted in [Figure 2d](#). It should be stressed that the ratio is found to be $\sim 0(10)$, that is, SFG can be dozens of times larger than SHG in the intensity. Low ratios in rt-TDDFT compared to the experiment may be caused by a lack of Coulomb interaction or a possible phonon-assisted mechanism (will be briefly discussed later) within the local density approximation (LDA). Adopting the results of [Figures 2c](#) and [2d](#), with nonlinear optical susceptibilities from the Greenwood–Kubo formalism based on Kohn–Sham orbitals, we can discuss dynamical details on SFG resulting in much more amplified nonlinear signals than SHG.

In [Figures 3a](#) and [3b](#), we demonstrate optical and SFG images taken as a function of the ω_1 -pulse wavelength for monolayer WSe₂ and WS₂ triangles grown by the molecular beam epitaxy (MBE) technique. A Raman spectrum for each monolayer TMD triangle indicated by the black arrow is available in the [Supporting Information](#). Since the SFG signal produced by two parallel linearly polarized pulses varies sample-to-sample according to the crystalline orientation, we select only the SFG signal along the polarization of the incident pulses using the analyzer. We find that SFG from 1L-WSe₂ at 740 nm (i.e., $\omega_1 = 1.68$ eV) is brightest, whereas SFG from 1L-WS₂ is one order of magnitude different from 1L-WSe₂ in the intensity ([Figure 3c](#)). It is then an essence to note that although SFG for 1L-WSe₂ satisfies the dual resonances at A and D excitons, SFG for 1L-WS₂ satisfies only a single resonance at D exciton in the present illumination. The ratio between two SFG susceptibilities ($= \chi_{\text{SFG}}^{(2)}[\text{WSe}_2]/\chi_{\text{SFG}}^{(2)}[\text{WS}_2]$) is evaluated to be 3.43 using the infinite sheet source model, which is revealed from $\chi_{\text{SFG}}^{(2)}[\text{WSe}_2] = 23$ nm/V and $\chi_{\text{SFG}}^{(2)}[\text{WS}_2] = 6.7$ nm/V. Optical absorption spectra of [Figure 3d](#) are obtained by taking the optical conductivity $\sigma_{yy}(\omega)$ of the Greenwood–Kubo equation given by, within the linear response,

$$\sigma_{yy}(\omega) = i \frac{e^2}{\hbar m_e} \sum_{\mathbf{k}} \sum_{nm} \frac{1}{E_m(\mathbf{k}) - E_n(\mathbf{k})} \times \left[\frac{\langle \Psi_{n\mathbf{k}} | p_y | \Psi_{m\mathbf{k}} \rangle \langle \Psi_{m\mathbf{k}} | p_y | \Psi_{n\mathbf{k}} \rangle}{\hbar\omega - E_m(\mathbf{k}) + E_n(\mathbf{k}) + i\delta} + \left(\frac{\langle \Psi_{n\mathbf{k}} | p_y | \Psi_{m\mathbf{k}} \rangle \langle \Psi_{m\mathbf{k}} | p_y | \Psi_{n\mathbf{k}} \rangle}{\hbar\omega - E_n(\mathbf{k}) + E_m(\mathbf{k}) + i\delta} \right)^* \right] \quad (2)$$

where n , m , and m_e stand for band indices of occupied, unoccupied states, and mass of electron, respectively, and the polarization of the incident pulses is assumed to be along the \hat{y} -direction. $E_n(\mathbf{k})$ and $|\Psi_{n\mathbf{k}}\rangle$ stand for the n -th band energy and the corresponding Kohn–Sham state at the momentum \mathbf{k} calculated from ELK code. The optical conductivity $\sigma_{yy}(\omega)$ can be directly converted into the electric susceptibility $\chi_{yy}(\omega)$ from the relation $\chi_{yy}(\omega) = i \sigma_{yy}(\omega)/\epsilon_0\omega^{35}$ which means that an imaginary part of the susceptibility is the real part of the optical conductivity. Now, the second-order nonlinear susceptibility induced by two incident pulses ω_1 and ω_2 could be approximately constructed from linear optical conductivities using Miller's rule such as by

$$\chi_{yy}^{(2)}(\omega_1, \omega_2) \propto \chi_{yy}(\omega_1)\chi_{yy}(\omega_2)\chi_{yy}(\omega_1 + \omega_2) \quad (3)$$

The nonlinear susceptibility $\chi_{yy}^{(2)}(\omega_1, \omega_2)$ in the dual resonant mode can then be eventually formulated as a function of ω_1 for a fixed ω_2 at 1.19 eV (i.e., 1040 nm) and spontaneously features an additional peak in the upper panel of [Figure 3e](#). In WSe₂, a simultaneous excitation of the two most singular resonances at A and D excitons enhances the SFG susceptibility.

In [Figures 4a](#) and [4b](#), we depict the momentum-dependent excitation energies of 1L-WSe₂ and 1L-WS₂ in terms of the energy differences between the conduction band minima (CBM) and the valence band maxima (VBM) along the K– Γ –M line of their electronic structures. One can easily find a main difference between the two materials. It is shown that WSe₂ has resonances split to C and D excitonic bands near the Δ point, whereas WS₂ has only a single resonance D at the same point (in fact, C exciton looks more or less suppressed). This directly affects behaviors of imaginary parts of susceptibilities in the two-dimensional reciprocal space as shown in [Figures 4c](#) and [4d](#). First, A and B excitonic resonances of WSe₂ and WS₂ are shown to be similar to each other due to the common characteristics of electronic structures of TMDs through $\text{Im}[\chi_{yy}^{(2)}(\mathbf{k}; \omega_A, \omega_2)]$ and $\text{Im}[\chi_{yy}^{(2)}(\mathbf{k}; \omega_B, \omega_2)]$. Second, C resonance of WSe₂ is shown to be circularly distributed around the Δ point through $\text{Im}[\chi_{yy}^{(2)}(\mathbf{k}; \omega_C, \omega_2)]$, but its existence is not very clear in WS₂. Lastly, D resonance due to the band nesting is distributed with the Γ point enclosed and weakly connected up to the Δ point in WSe₂ and similarly but robustly continues to the Δ point in WS₂ as shown in plots of $\text{Im}[\chi_{yy}^{(2)}(\mathbf{k}; \omega_D, \omega_2)]$. Meanwhile, it is known that the electron–phonon coupling between conduction electrons and longitudinal acoustic modes of TMDs is highly damped between momenta at the K and Γ points.³⁶ In a viewpoint of the momentum transfer, it may then imply that the small electron–phonon scattering could readily assist coherent electrons to be efficiently deployed between A and D resonances, which would enhance the dual resonance during

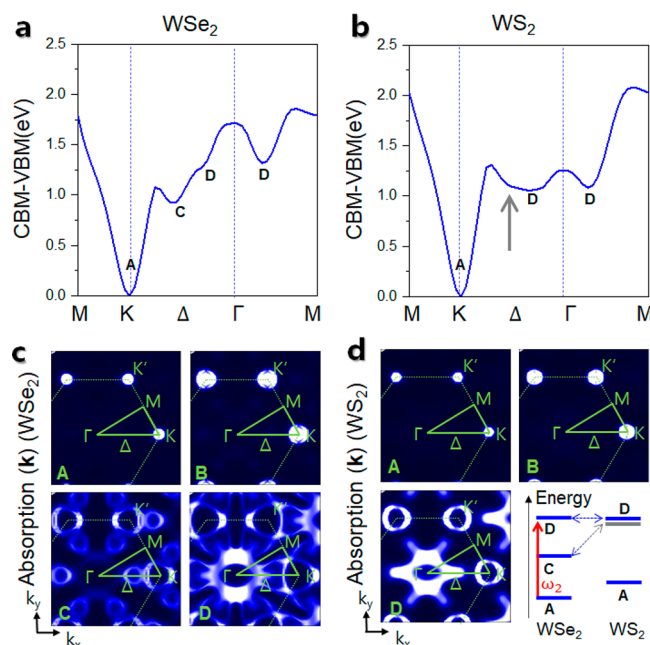


Figure 4. Nonlinear excitonic dynamics of 1L-WSe₂ and 1L-WS₂. (a, b) Momentum-dependent excitation energy given by the difference between CBM and VBM. A, C, and D mean A, C, and D excitons, respectively. The gray arrow indicates a dim footprint of C exciton in 1L-WS₂. (c, d) Momentum-resolved susceptibility spectra of each resonance in 1L-WSe₂ and 1L-WS₂. Concerning A, B, C, and D excitonic resonances, $\text{Im}[\chi_{yy}^{(2)}(\mathbf{k}; \omega_A, \omega_2)]$, $\text{Im}[\chi_{yy}^{(2)}(\mathbf{k}; \omega_B, \omega_2)]$, $\text{Im}[\chi_{yy}^{(2)}(\mathbf{k}; \omega_C, \omega_2)]$, and $\text{Im}[\chi_{yy}^{(2)}(\mathbf{k}; \omega_D, \omega_2)]$ are plotted, respectively. A schematic in the bottom-right panel of (d) represents a different resonant structure between WSe₂ and WS₂. The gray level implies a footprint of C exciton in WS₂.

the optically nonequilibrium states. This would be rather reinforced by separate resonances of C and D observed in WSe₂. Compared with WSe₂, a dim footprint of C resonance near the similar position (pointed by the gray arrow of Figure 4b) may be also indicated in WS₂ (Figure 4d).

CONCLUSIONS

We proposed the dual resonant optical SFG to select the two most singular resonances and then reported for 1L-WSe₂ when one (ω_1) of the excitation pulses was resonant to the direct band gap (A exciton) and their sum frequency ($\omega_1 + \omega_2$) to the band nesting (D exciton). The timely stretched nature of SFG was captured by tracking temporal overlap of the two excitation pulses, disclosing the pulse duration time to be ~ 360 fs, of which time-dependent cross-correlation was critically evaluated with Mach–Zehnder interferometry. The second-order SFG susceptibility $= \chi_{\text{SFG}}^{(2)}$ of 1L-WSe₂ was experimentally determined to be 23 nm/V at the dual resonant mode and 10 nm/V at the slight off-dual-resonant mode where the optical second harmonic generation (SHG) is resonant, i.e., $2\omega_1$ to the D excitonic absorption. SFG was also found to be about 20 times more efficient than SHG for the same fluence $\sim 1.4 \times 10^{10}$ W/m² of the ω_1 and ω_2 pulses, which was theoretically reproduced by the time-evolution of Kohn–Sham orbitals within rt-TDDFT. Further, the dual resonant SFG susceptibility of 1L-WSe₂ was found as high as 23 nm/V. This should be compared with the single resonant SFG of 1L-WS₂, whose susceptibility remained to be 6.7 nm/V. Finally, in the two-dimensional reciprocal space, the momentum transfer efficacy

of 1L-WSe₂ and 1L-WS₂ was discussed based on the nonlinear optical responses constructed from the Greenwood–Kubo formalism. Our results provide exciting insights on the TMD-based nonlinear optics and optical device technology as well as the nonlinear spectroscopy and microscopy for two-dimensional quantum materials.

ASSOCIATED CONTENT

Supporting Information

The Supporting Information is available free of charge at <https://pubs.acs.org/doi/10.1021/acs.nanolett.0c01363>.

Schematic diagram for the Mach–Zehnder-type SFG interferometry (Figure S1), interferogram of SFG from the WSe₂ monolayer (Figure S2), Raman spectroscopy on WSe₂ and WS₂ atomic monolayers (Figure S3), calculation details on first-principles rt-TDDFT, optical absorption (imaginary part of optical susceptibility) obtained from the Greenwood–Kubo formalism for WSe₂ and WS₂ atomic monolayers (Figure S4), frequency-dependent intensity profiles of SFG and SHG (Figure S5), fitting the A resonance to shorter wavelength and modified SFG intensity (Figure S6), rt-TDDFT calculation of the SFG intensity with respect to the ω_2 pulse fluence at a fixed ω_1 pulse fluence (Figure S7), and ω_1 -dependent single resonant SFG intensity at a fixed sum frequency resonant to D exciton (Figure S8) (PDF)

AUTHOR INFORMATION

Corresponding Authors

Hyunmin Kim – Division of Biotechnology, DGIST, Daegu 42988, Republic of Korea; orcid.org/0000-0002-9338-4597; Email: hyunmin.kim@dgist.ac.kr

J.D. Lee – Department of Emerging Materials Science, DGIST, Daegu 42988, Republic of Korea; Email: jdlee@dgist.ac.kr

Authors

Youngjae Kim – Department of Emerging Materials Science, DGIST, Daegu 42988, Republic of Korea; orcid.org/0000-0002-4544-2940

Houk Jang – School of Engineering and Applied Sciences, Harvard University, Cambridge, Massachusetts 02138, United States

Jong-Hyun Ahn – School of Electrical and Electronic Engineering, Yonsei University, Seoul 03722, Republic of Korea; orcid.org/0000-0002-8135-7719

Complete contact information is available at: <https://pubs.acs.org/doi/10.1021/acs.nanolett.0c01363>

Author Contributions

H.K. and J.D.L. materialized the research idea. Y.K. carried out theoretical calculations, and Y.K. and J.D.L. discussed theoretical results. H.K. performed sample preparation and optical experiments. Y.K., H.K., and J.D.L. wrote the manuscript. H.J. and J.-H.A. participated in sample preparation and optical experiments.

Notes

The authors declare no competing financial interest.

ACKNOWLEDGMENTS

This work was supported by the Basic Science Research Program (2019R1A2C1005050, 2017K1A3A1A1907045513)

through the National Research Foundation of Korea (NRF) and also by the DGIST R&D program (20-CoE-NT-01), funded by the Ministry of Science and ICT.

REFERENCES

- (1) Kumar, N.; Najmaei, S.; Cui, Q.; Ceballos, F.; Ajayan, P. M.; Lou, J.; Zhao, H. Second harmonic microscopy of monolayer MoS₂. *Phys. Rev. B: Condens. Matter Mater. Phys.* **2013**, *87*, No. 161403(R).
- (2) Sutherland, R.L. *Handbook of Nonlinear Optics*; Marcel Dekker, Inc.: New York, 2003.
- (3) Zhao, M.; Ye, Z.; Suzuki, R.; Ye, Y.; Zhu, H.; Xiao, J.; Wang, Y.; Iwasa, Y.; Zhang, X. Atomically phase-matched second-harmonic generation in a 2D crystal. *Light: Sci. Appl.* **2016**, *5*, No. e16131.
- (4) Hardhienata, H.; Alejo-Molina, A.; Reitböck, C.; Prylepa, A.; Stifter, D.; Hingerl, K. Bulk dipolar contribution to second-harmonic generation in zincblende. *J. Opt. Soc. Am. B* **2016**, *33* (2), 195–201.
- (5) Malard, L. M.; Alencar, T. V.; Barboza, A. P. M.; Mak, K. F.; de Paula, A. M. Observation of intense second harmonic generation from MoS₂ atomic crystals. *Phys. Rev. B: Condens. Matter Mater. Phys.* **2013**, *87*, No. 201401(R).
- (6) Clark, D. J.; Senthilkumar, V.; Le, C. T.; Weerawarne, D. L.; Shim, B.; Jang, J. I.; Shim, J. H.; Cho, J.; Sim, Y.; Seong, M.-J.; Rhim, S. H.; Freeman, A. J.; Chung, K.-H.; Kim, Y. S. Strong optical nonlinearity of CVD-grown MoS₂ monolayer as probed by wavelength-dependent second-harmonic generation. *Phys. Rev. B: Condens. Matter Mater. Phys.* **2014**, *90*, No. 121409(R).
- (7) Ribeiro-Soares, J.; Janisch, C.; Liu, Z.; Elías, A. L.; Dresselhaus, M. S.; Terrones, M.; Cançado, L. G.; Jorio, A. Second Harmonic Generation in WSe₂. *2D Mater.* **2015**, *2*, 045015.
- (8) Janisch, C.; Wang, Y.; Ma, D.; Mehta, N.; Elías, A. L.; Perea-López, N.; Terrones, M.; Crespi, V.; Liu, Z. Extraordinary Second Harmonic Generation in Tungsten Disulfide Monolayers. *Sci. Rep.* **2015**, *4*, 5530.
- (9) Wang, G.; Marie, X.; Gerber, I.; Amand, T.; Lagarde, D.; Bouet, L.; Vidal, M.; Balocchi, A.; Urbaszek, B. Giant Enhancement of the Optical Second-Harmonic Emission of WSe₂ Monolayers by Laser Excitation at Exciton Resonances. *Phys. Rev. Lett.* **2015**, *114*, 097403.
- (10) Lin, K.-Q.; Bange, S.; Lupton, J. M. Quantum interference in second-harmonic generation from monolayer WSe₂. *Nat. Phys.* **2019**, *15*, 242–246.
- (11) Li, D.; Xiong, W.; Jiang, L.; Xiao, Z.; Rabiee Golgir, H.; Wang, M.; Huang, X.; Zhou, Y.; Lin, Z.; Song, J.; Ducharme, S.; Jiang, L.; Silvain, J.-F.; Lu, Y. Multimodal Nonlinear Optical Imaging of MoS₂ and MoS₂-Based van der Waals Heterostructures. *ACS Nano* **2016**, *10* (3), 3766–3775.
- (12) Yao, K.; Yanev, E.; Chuang, H.-J.; Rosenberger, M. R.; Xu, X.; Darlington, T.; McCreary, K. M.; Hanbicki, A. T.; Watanabe, K.; Taniguchi, T.; Jonker, B. T.; Zhu, X.; Basov, D. N.; Hone, J. C.; Schuck, P. J. Continuous Wave Sum Frequency Generation and Imaging of Monolayer and Heterobilayer Two-Dimensional Semiconductors. *ACS Nano* **2020**, *14* (1), 708–714.
- (13) Tamaya, T.; Ishikawa, A.; Ogawa, T.; Tanaka, K. Diabatic Mechanisms of Higher-Order Harmonic Generation in Solid-State Materials under High-Intensity Electric Fields. *Phys. Rev. Lett.* **2016**, *116*, 016601.
- (14) Tamaya, T.; Kato, T. Subband picture of high-harmonic generation in solids. *Phys. Rev. B: Condens. Matter Mater. Phys.* **2019**, *100*, No. 081203(R).
- (15) Otake, T. High-harmonic generation in α -quartz by electron-hole recombination. *Phys. Rev. B: Condens. Matter Mater. Phys.* **2016**, *94*, 235152.
- (16) Tancogne-Dejean, N.; Mücke, O. D.; Kärtner, F. X.; Rubio, A. Impact of the Electronic Band Structure in High-Harmonic Generation Spectra of Solids. *Phys. Rev. Lett.* **2017**, *118*, 087403.
- (17) Lian, C.; Guan, M.; Hu, S.; Zhang, J.; Meng, S. Photoexcitation in Solids: First-Principles Quantum Simulations by Real-Time TDDFT. *Adv. Theory Simul.* **2018**, *1*, 1800055.
- (18) Guan, M.-X.; Lian, C.; Hu, S.-Q.; Liu, H.; Zhang, S.-J.; Zhang, J.; Meng, S. Cooperative evolution of intraband and interband excitations for high-harmonic generation in strained MoS₂. *Phys. Rev. B: Condens. Matter Mater. Phys.* **2019**, *99*, 184306.
- (19) Tancogne-Dejean, N.; Sentef, M. A.; Rubio, A. Ultrafast Modification of Hubbard U in a Strongly Correlated Material: Ab initio High-Harmonic Generation in NiO. *Phys. Rev. Lett.* **2018**, *121*, 097402.
- (20) Le Breton, G.; Rubio, A.; Tancogne-Dejean, N. High-harmonic generation from few-layer hexagonal boron nitride: Evolution from monolayer to bulk response. *Phys. Rev. B: Condens. Matter Mater. Phys.* **2018**, *98*, 165308.
- (21) Qin, R.; Chen, Z.-Y. Strain-controlled high harmonic generation with Dirac fermions in silicene. *Nanoscale* **2018**, *10*, 22593–22600.
- (22) Rathgen, H.; Katsnelson, M. I. Symmetry Assumptions, Kramers-Kronig Transformation and Analytical Continuation in Ab Initio Calculations of Optical Conductivities. *Phys. Scr.* **2004**, *T109*, 170–174.
- (23) Mannebach, E. M.; Duerloo, K.-A. N.; Pellouchoud, L. A.; Sher, M.-J.; Nah, S.; Kuo, Y.-H.; Yu, Y.; Marshall, A. F.; Cao, L.; Reed, E. J.; Lindenberg, A. M. Ultrafast Electronic and Structural Response of Monolayer MoS₂ under Intense Photoexcitation Conditions. *ACS Nano* **2014**, *8* (10), 10734–10742.
- (24) Hell, S. W.; Wichmann, J. Breaking the diffraction resolution limit by stimulated emission: Stimulated-emission-depletion fluorescence microscopy. *Opt. Lett.* **1994**, *19* (11), 780–782.
- (25) Hein, B.; Willig, K. I.; Hell, S. W. Stimulated emission depletion (STED) nanoscopy of a fluorescent protein-labeled organelle inside a living cell. *Proc. Natl. Acad. Sci. U. S. A.* **2008**, *105* (38), 14271–14276.
- (26) Venezuela, P.; Lazzeri, M.; Mauri, F. Theory of double-resonant Raman spectra in graphene: Intensity and line shape of defect-induced and two-phonon bands. *Phys. Rev. B: Condens. Matter Mater. Phys.* **2011**, *84*, 035433.
- (27) Ferrari, A. C.; Basko, D. M. Raman spectroscopy as a versatile tool for studying the properties of graphene. *Nat. Nanotechnol.* **2013**, *8*, 235–246.
- (28) Yoon, D.; Son, Y.-W.; Cheong, H. Strain-Dependent Splitting of the Double-Resonance Raman Scattering Band in Graphene. *Phys. Rev. Lett.* **2011**, *106*, 155502.
- (29) Wang, K.; Huang, B.; Tian, M.; Ceballos, F.; Lin, M.-W.; Mahjouri-Samani, M.; Boulebaa, A.; Puzos, A. A.; Rouleau, C. M.; Yoon, M.; Zhao, H.; Xiao, K.; Düscher, G.; Geoegean, D. B. Interlayer Coupling in Twisted WSe₂/WS₂ Bilayer Heterostructures Revealed by Optical Spectroscopy. *ACS Nano* **2016**, *10* (7), 6612–6622.
- (30) Jang, H.; Dhakal, K. P.; Joo, K.-I.; Yun, W. S.; Shinde, S. M.; Chen, X.; Jeong, S. M.; Lee, S. W.; Lee, Z.; Lee, J. D.; Ahn, J.-H.; Kim, H. Carrier Dynamics: Transient SHG Imaging on Ultrafast Carrier Dynamics of MoS₂ Nanosheets. *Adv. Mater.* **2018**, *30*, 1705190.
- (31) Dhakal, K. P.; Kim, H.; Lee, S.; Kim, Y.; Lee, J. D.; Ahn, J.-H. Probing the upper band gap of atomic rhenium disulfide layers. *Light: Sci. Appl.* **2018**, *7*, 98.
- (32) Yampolsky, S.; Fishman, D. A.; Dey, S.; Hulkko, E.; Banik, M.; Potma, E. O.; Apkarian, V. A. Seeing a single molecule vibrate through time-resolved coherent anti-Stokes Raman scattering. *Nat. Photonics* **2014**, *8*, 650–656.
- (33) Malitson, I. H. Interspecimen Comparison of the Refractive Index of Fused Silica. *J. Opt. Soc. Am.* **1965**, *55*, 1205–1208.
- (34) Li, Y.; Rao, Y.; Mak, K. F.; You, Y.; Wang, S.; Dean, C. R.; Heinz, T. F. Probing Symmetry Properties of Few-Layer MoS₂ and h-BN by Optical Second-Harmonic Generation. *Nano Lett.* **2013**, *13* (7), 3329–3333.
- (35) Martin, R. M. *Electronic Structure Basic Theory and Practical Methods*; Cambridge University Press: New York, 2004.
- (36) Guo, F.; Liu, Z.; Zhu, M.; Zheng, Y. Electron-phonon scattering limited hole mobility at room temperature in a MoS₂ monolayer: first-principles calculations. *Phys. Chem. Chem. Phys.* **2019**, *21*, 22879.